J|A|C|S ARTICLES

Published on Web 04/22/2009

Emission Mechanism of Doubly *ortho*-Linked Quinoxaline/Diphenylfluorene or *cis*-Stilbene/Fluorene Hybrid Compounds Based on the Transient Absorption and Emission Measurements during Pulse Radiolysis

Yi Wei,[†,‡] Shingo Samori,[‡] Sachiko Tojo,[‡] Mamoru Fujitsuka,[‡] Jin-Sheng Lin,[†] Chien-Tien Chen,*[,†] and Tetsuro Majima*[,‡]

Department of Chemistry, National Taiwan Normal University, Taipei, Taiwan 11650, and the Institute of Scientific and Industrial Research (SANKEN), Osaka University, Mihogaoka 8-1, Ibaraki, Osaka 567-0047, Japan

Received November 17, 2008; E-mail: chefv043@ntnu.edu.tw; majima@sanken.osaka-u.ac.jp

Abstract: A series of bipolar OLED materials were subjected to pulsed radiolysis experiments to determine their transient absorption and lifetime profiles of the independently in situ generated radical cations and anions in solutions. Moreover, their emission behaviors from the charge recombination of their radical ions were also determined by the pulse radiolysis method. It was found the absorption bands in doubly *ortho*-linked quinoxaline/diphenylfluorene hybrids **1a**−**e** are red-shifted progressively with increasing electron-donating nature at the C5 and C8 positions of the quinoxaline template. The incipient radical anions in **1a**−**e** are mainly localized on the quinoxaline heterocyclic moiety, whereas the incipient radical cations are mainly distributed onto the attached electron-donating groups at the C5 and C8 positions of the quinoxaline template. For other doubly *ortho*-linked *cis*-stilbene derivatives **3d**, **3f**, and **4f**, the radical anions are mainly localized on the *cis*-stilbene central moiety and the radical cation is mainly distributed onto both *para* substituents of the *cis*-stilbene templates. It was also shown that there is a correlation between their optoelectronic emission efficiencies and the radiolysis induced emission intensities. In addition, the charge transporting behaviors within an OLED device were found to show the relationship with transient absorption half-lives ($\tau_{1/2}$) of the radical ions. Charge recombination mechanisms in both the OLED and pulsed radiolysis experiments were proposed to rationalize these observations, allowing us to establish some guidelines for an ultimate molecular design of ideal bipolar optoelectronic materials with a judicious choice of local charge appendages in the optoelectronic templates.

1. Introduction

Various highly efficient electroluminescence (EL) materials have been explored over the past two decades in lieu of their potential uses in organic light-emitting diodes (OLED) in flat-panel display technology.[1] Particularly, tremendous attention has been paid to bipolar fluorescent materials with integrated donor and acceptor moieties in view of their much more balanced charge transports, simplification of device fabrication, and ultimate potentials in single layer devices.[2] The doubly *ortho*-linked quinoxaline/diphenylfluorene hybrid OLED materials developed by us have shown highly efficient fluorescence profiles with tunable full spectrum of B-G-Y-R colors. In addition, we recently found that configurationally confined donor-substituted *cis*-stilbene/fluorene hybrids are promising hole-transport type blue emitters.

By understanding the emission mechanism in solution for bipolar compounds as the efficient OLED materials, one may achieve better design of molecular materials with optimal optoelectronic efficiencies. We have recently examined the emission spectra of various bipolar molecules bearing a 9-cyanoanthrcenyl unit by electrogenerated chemiluminescence (ECL) or thru intermolecular electron transfer from a respective radical anion to a proximal radical cation during pulse radiolysis in benzene.[3] It was found that the pulse radiolysis technique was able to clarify the emission mechanism of these bipolar type molecules which exhibit fluorescent characters. In addition, it was found there is a direct correlation between the ECL and the radiolysis induced emission. Chen and co-workers recently developed a series of efficient bipolar OLED materials derived

[†] National Taiwan Normal University.
[‡] Osaka University.

(1) (a) Mullen, K.; Scherf, U.; *Organic Light-Emitting Devices. Synthesis, Properties and Applications*; Wiley: Weinheim, Germany, 2006. (b) Burroughes, J. H.; Bradley, D. D. C.; Brown, A. R.; Marks, R. N.; Mackay, K.; Friend, R. H.; Burns, P. L.; Holmes, A. B. *Nature (London)* **1990**, *347*, 539. (c) Chen, C.-H.; Huang, S.-W. *OLED/Organic Electroluminescent Materials & Devices*; Wunan: Taipei, Taiwan, 2006.

(2) (a) Yeh, H.-C.; Yeh, S.-J.; Chen, C.-T. *Chem. Commun.* **2003**, 2632. (b) Thomas, K. R. J.; Lin, J.-T.; Tao, Y.-T.; Chuen, C.-H. *Chem. Mater.* **2002**, *14*, 2796. (c) Huang, T.-H.; Lin, J.-T.; Chen, L.-Y.; Lin, Y.-T.; Wu, C.-C. *Adv. Mater.* **2002**, *18*, 602. (d) Kim, D. U.; Paik, S. H.; Kim, S. H.; Tsutsui, T. *Synth. Met.* **2001**, *123*, 43.

(3) (a) Samori, S.; Tojo, S.; Fujitsuka, M.; Yang, S.-W.; Elangoven, A.; Ho, T.-I.; Majima, T. *J. Org. Chem.* **2005**, *70*, 6661. (b) Samori, S.; Tojo, S.; Fujitsuka, M.; Liang, H.-J.; Ho, T.-I.; Yang, J.-S.; Majima, T. *J. Org. Chem.* **2006**, *71*, 8732. (c) Samori, S.; Tojo, S.; Fujitsuka, M.; Yang, S.-W.; Ho, T.-I.; Yang, J.-S.; Majima, T. *J. Phys. Chem. B* **2006**, *110*, 13296.

 10.1021/ja8090005 CCC: $40.75

Scheme 1. Materials with Integrated Donor and/or Acceptor Moieties (**1** and **3**) and Their Reference Compounds (**2** and **4**)

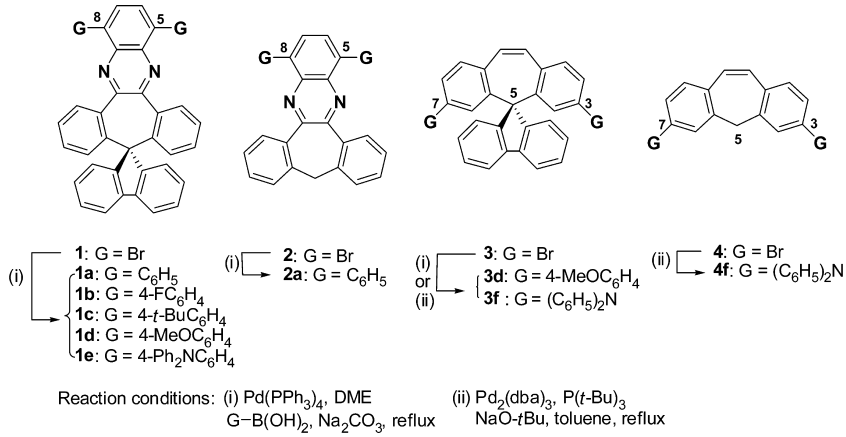

from an electron-accepting quinoxaline-fused dibenzosuberene (DBE) core with a spiro-fluorene damper and electron-donating aryl groups at both C5 and C8 positions. These compounds serve as fluorescent "chameleon" type materials with tunable R-G-Y-B emission colors (**1a**−**e** in Scheme 1). They exhibit high fluorescent efficiencies in the OLED devices.[4] However, the origins for their excellent optoelectronic performance remain to be understood. The formation of excited states in the solid state by the application of an electric field (as in OLED) has been shown to follow a mechanism similar to that in solution (ECL).[5] Therefore, we sought to examine if we can directly correlate the emission mechanisms by pulse radiolysis technique with those through electroluminescent measurements in OLED. By unraveling the emission mechanisms of these materials in solid states in OLED, one may achieve designing even more advanced molecular materials with optimal optoelectronic performances.

To have an in-depth study on the operating EL mechanism of the compounds for the efficient OLED materials, a series of these derivatives **1a**−**e** (Scheme 1) with varying aryl substitutions were chosen and investigated by a pulse radiolysis technique. Furthermore, sky-blue emitting materials (**3d** and **3f**) derived from spirally linked *cis*-stilbene were also examined.[6] Compounds **2a** and **4f** which lack the spiro fluorene damper were used as reference materials for comparisons in each series, respectively.

2. Experimental Section

All reagents and solvents were commercially available and were purified before use.

2.1. Materials Syntheses. The syntheses of compounds **1**−**4** were summarized in the Supporting Information, and their structural identities were confirmed by NMR spectroscopic and/or X-ray crystallographic analyses.

2.2. Steady-State Photophysical Measurements. Absorption spectra were measured on an HP-8453 Diode Array spectrometer by using spectrophotometric grade CH_2Cl_2. Emission spectra (in 10 μM) were measured on an Aminco-Bowman Series 2 luminescence spectrometer upon excitation at the absorption maxima of the longest absorption band in the same solvent. The emission spectra were normalized by their emission maxima to the same intensity (maximum intensity = 1). Quantum yield (Φ_f, %) measurements were performed by using Coumarin-1[7] (99%, EtOAc), Coumarin-6[8] (78%, EtOH), and DCM[9] (65%, CH_3CN) as standards.

2.3. Cyclic Voltammetry (CV) Measurements. CV experiments were carried out with 1.0 mM of one substrate in a given anhydrous, degassed solvent containing 0.1 M tetrabutylammonium perchlorate (n-Bu_4NClO_4) as a supporting electrolyte on a Chinstruments CH1604A potentiostat. A platinum electrode was used as a counter electrode, and a carbon electrode was used as a working electrode. Ag/AgCl was used as a reference electrode.

2.4. Differential Scanning Calorimetry (DSC) Analyses. DSC measurements were performed on a SEIKO SSC 5200 DSC Computer/Thermal Analyzer. The samples were first heated (20 °C/min) to melt and then quenched with liquid nitrogen. Glass transition temperatures (T_g) were recorded by heating (10 °C/min) the cooled samples.

2.5. Thermogravimetric Analyses (TGA). TGA measurements were performed on a SEIKO TG/DTA200 instrument by the Northern Instrument Center of Taiwan. Melting points were measured on a Hargo MP-2D instrument.

2.6. Device Fabrication and Measurements. All the materials were either commercially available or synthesized as described in our previous publications and were subjected to gradient sublimation under high vacuum prior to use. The substrate was an indium tin oxide (ITO) coated glass with a sheer resistance of ~30 Ω/□. Prepatterned ITO substrates were cleaned sequentially by sonication in a detergent solution, doubly distilled water, and EtOH for 5 min in turn before being blown dry with a stream of nitrogen. The ITO substrate was then treated with oxygen plasma for 5 min before being loaded into the vacuum chamber. The organic layers were deposited thermally at a rate of 0.1−0.3 nm/s in a chamber (ULVAC, TU-12RE) under a pressure of 5×10^{-6} Torr. Devices were constructed with a 40 nm thickness of NPB as the hole-transporting layer (HTL), 40 nm of emitter as the light-emitting layer (LEL), 40 nm of Alq_3 or TPBI as the electron-transporting layer (ETL), 10 nm of BCP as the hole-blocking layer (HBL), 1 nm of LiF as the electron-injecting layer (EIL), and 150 nm of Al as the cathode, respectively. Current−voltage−light intensity (I−V−L) characteristics and EL spectra were measured and recorded by PRECISE GAUGE, EL-1003. Lifetime (i.e., the time needed to induce 50% decrease in luminance intensity) measurements were carried out at 20 mA/cm^2 by using compound **1e** for

(4) Chen, C.-T.; Wei, Y.; Lin, J.-S.; Moturu, M. V. R. K.; Chao, W.-S.; Tao, Y.-T.; Chien, C.-H. *J. Am. Chem. Soc.* **2006**, *128*, 10992.
(5) (a) Anderson, J. D.; et al. *J. Am. Chem. Soc.* **1998**, *120*, 9646. (b) Armstrong, N. R.; Anderson, J. D.; Lee, P. A.; McDonald, E. M.; Wightman, R. M.; Hall, H. K.; Hopkins, T.; Padias, A.; Thayumanavan, S.; Barlow, S.; Marder, S. R. *SPIE* **1999**, *3476*, 178. (c) Armstrong, N. R.; Whightman, R. M.; Gross, E. M. *Annu. Rev. Phys. Chem.* **2001**, *52*, 391.
(6) Wei, Y.; Chen, C.-T. *J. Am. Chem. Soc.* **2007**, *129*, 7478.
(7) Jones, G. II; Jackson, W. R.; Choi, C.-Y.; Bergmark, W. R. *J. Phys. Chem.* **1985**, *89*, 294.
(8) Reynolds, G. A.; Drexhage, K. H. *Opt. Commun.* **1975**, *13*, 222.
(9) Tang, C. W.; VanSlyke, S. A. *J. Appl. Phys.* **1989**, *65*, 3610.

device-**C**. In addition, the lifetime of Alq_3 for a standard device-**A** (i.e., ITO/NPB(40 nm)/Alq_3(40 nm)/LiF(1 nm)/Al) was measured at the same current density for comparison. All the measurements were made at atmospheric conditions.

2.7. Pulse Radiolysis Measurements. Pulse radiolysis experiments were performed by using an electron pulse (28 MeV, 8 ns, 0.87 kGy per pulse) from a linear accelerator at Osaka University. All sample solutions were prepared at the concentration of 5 mM in a given solvent in a rectangular quartz cell (0.5 × 1.0 × 4.0 cm^3, path length of 1.0 cm). These solutions were saturated with Ar gas by bubbling with a continuous stream of Ar thru the solutions for 10 min at ambient temperature before irradiation. The kinetic measurements were performed using a nanosecond photoreaction analyzer system (Unisoku, TSP-1000). The monitor light was obtained from a pulsed 450 W Xe arc lamp (Ushio, UXL-451-0), which was operated by a large current pulsed-power supply that was synchronized with the electron pulse. The monitor light was passed through an iris with a diameter of 0.2 cm and directed into the sample solution perpendicular to the electron pulse. The monitor light passing through the sample was focused on the entrance slit of a monochromator (Unisoku, MD200) and detected with a photomultiplier tube (Hamamatsu Photonics, R2949). The transient absorption and emission spectra were measured by using a photodiode array (Hamamatsu Photonics, S3904-1024F) with a gated image intensifier (Hamamatsu Photonics, C2925-01) as a detector. All emission spectra were corrected for the spectral sensitivity of the apparatus. To avoid pyrolysis of the sample solution by monitor light, a suitable cutoff filter was used.

3. Results

3.1. Synthesis and Characterization. The syntheses of compounds **1c**−**e**, **3f**, and **4f** have been described in our previous publications. The others were synthesized similarly by Suzuki coupling reactions of suitable arylboronic acids with the individual central dibromide templates **1** and **3** in good yields (89−95%).[10] The structural identites for **1a** and **3d** were further confirmed by X-ray crystallographic analyses. Both the phenyl groups in **1a** are twisted by +49.5 and −49.7°, respectively (Figure 1a), relative to the quinoxoline template to prevent unfavorable *epi*-interaction with quinoxaline nitrogen lone pairs. On the other hand, the 4-methoxyphenyl appendages in **3d** are twisted by 15.6° and −5.8°, respectively (Figure 1b) with partial conjugation with a central *cis*-stilbene template.

In the first system (**1a**−**e**), the substituents at the C5 and C8 positions of quinoxaline moiety are divided into three classes, including (1) the parent phenyl group for **1a** (G = Ph), (2) an electron-withdrawing (EWG) *para*-substituted aryl groups for **1b** (G = 4-fluorophenyl), and (3) electron-donating (EDG) *para*-substituted aryl groups for **1c**−**e** (i.e., G = 4-*tert*-butylC_6H_4 for **1c**, G = 4-MeOC_6H_4 for **1d**, and G = 4-$Ph_2NC_6H_4$ for **1e**, respectively). For the second system (**3d**,**f**), the substituents at the C3 and C7 positions of dibenzosuberene (DBE) moiety are all electron-donating (i.e., G = 4-MeOC_6H_4 for **3d** and G = $(C_6H_5)_2N$ for **3f**, respectively) aryl groups. The rigid butterfly shaped structure with a spiral tail not only prevents facile conformational flipping of the central seven-membered ring in the DBE core but also avoids intermolecular parallel $\pi-\pi$ stacking (vide infra).

3.2. Steady-State Photophysical and Thermostability Properties. Figure 2 shows the UV−vis absorption and emission stacked plots for **1a**−**e** and **2a** (a) and **3d**, **3f**, and **4f** (b) by the steady-state measurements in Ar-saturated CH_2Cl_2. Some important photophysical features for these compounds are compiled in Table 1. Notably, the resonance conjugations between the donor moieties in the pendant aryl groups and the quinoxaline backbone for **1a**−**e** are prominent in solution, exerting progressive, bathochromic shifts in their UV (361→441 nm) and photoluminescence (461→599 nm) spectra. Upon UV excitation, these materials show the emission colors in solution varying from blue, green, to orange. The full width at half-maximum (fwhm) for each individual emission also increases progressively from 71, 72, 74, 89, to 95 nm, with quantum yields ranging from 21 to 78%. A similar trend of bathochromic shifts (with increasing ICT) both in UV and emission λ_{max} (by 41 nm) was also observed from **3d** to **3f**. In addition, the incorporation of a spiral fluorene damper imposes a better coplanarity in the central *cis*-stilbene template in view of the significant red shifts in UV (by 36 nm) and emission (by 21 nm) λ_{max} from **4f** to **3f**. Mainly sky-blue emission was observed in the latter system.

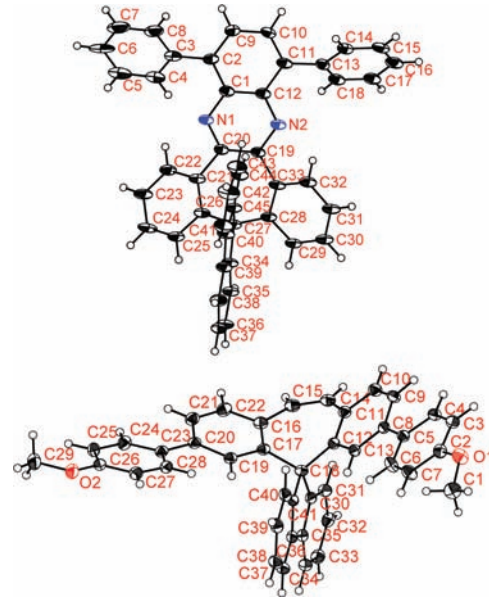

Figure 1. ORTEP diagrams for X-ray crystal structures (ellipsoids are shown at 30% probability level) for (a) **1a** (top) and (b) **3d** (bottom).

3.3. OLED Devices. The optoelectronic performances of these compounds were measured by fabricating OLED devices with these materials as the electron-transporting (ET) and emitting layer (**1a**−**e** for Device-A), hole-transporting (HT) and emitting layer (**1c**−**e** for Device-B; **3d**, **3f**, and **4f** for Device-D), and emitting layer (**1e** for Device-C; **3d** for Device-E, Table 2). Except in the cases of **1a**−**c** in device-A, the optoelectronic performances are excellent in terms of both the emission colors and device efficiencies. Despite that they share a common bichromophoric spiral template, the optoelectronic performances for **1a**−**e** change significantly with varying aryl substitutions at the C5 and C8 positions attached to the quinoxaline backbones. Emissions with initial intramolecular, chromophoric−chromophoric energy transfer between the two nearly perpendicular, spiral fragments (i.e., between the DBE and the fluorene templates) might be operable in view of their nontotally

(10) See the Supporting Information for details and the syntheses for **1**−**4**.

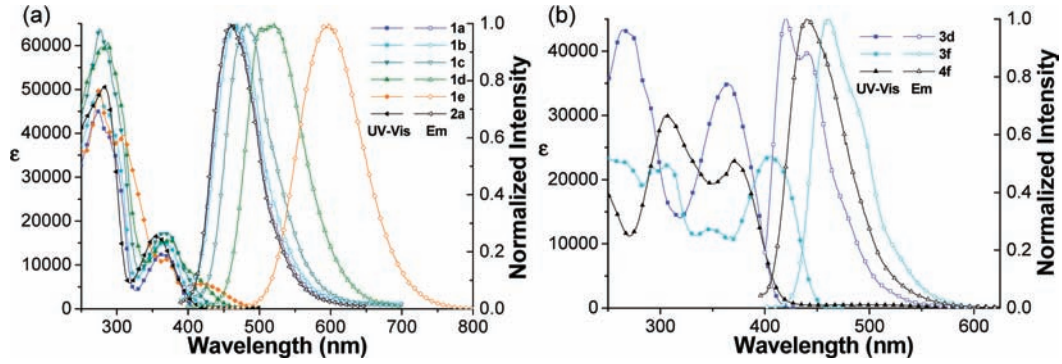

Figure 2. Stacked plots of UV−vis absorption and emission spectra of **1a**−**e** and **2a** (a) and **3d**, **3f**, and **4f** (b) by steady-state measurements in Ar-saturated CH_2Cl_2.

Table 1. Optical and Morphological Data for **1a**−**e**, **2a**, **3d**, **3f**, and **4f**

Compd	Abs. λ_{max}[a] ($\varepsilon \times 10^{-3}$)[b] (nm)	Em., λ_{max}[a,c] (nm)	Φ_f[d] (%)	T_g/T_d (°C)
1a	274(44.1), 361(16.7)	461 (71)	21	162/361
1b	275(49.5), 367(15.1)	469 (72)	34	161/362
1c	276(63.8), 367(17.2)	482 (74)	41	181/395
1d	288(60.6), 374(15.7)	521 (89)	78	160/372
1e	370(1.4), 441(3.6)	599 (95)	34	186/412
2a	283(50.5), 355(16.5)	462 (72)	21	98/377
3d	254(43.3), 365(35.0)	420, 454 (55)	80	118/411
3f	349(12.3), 406(23.6)	461 (57)	90	123/443
4f	306(22.9), 370(23.0)	440 (62)	99	101/397

[a] Peak maxima measured in CH_2Cl_2. [b] Molar absorption coefficient. [c] The data in parentheses correspond to full width at half-maximum (fwhm). [d] Fluorescence quantum yield determined by steady-state measurements.

symmetric vibronic coupling at low-lying excited states.[11] By comparing similar emission performances between **3f** and **4f** in device-D, we can conclude that it plays a negligible role in contributing to the fluorescent emissions observed.

It should be noted that the EL spectra obtained in OLED devices-A fabricated from **1a**,**b** showed λ_{max} at 548 and 562 nm, respectively (Figure 3a). Since the spectral shape of emissions changed with varying concentrations, they might be affected by self-absorption at the shorter wavelength region due to higher concentrations (Figure 4). Moreover, when absorptions of the devices exist up to 550 nm, the self-absorption occurs efficiently and the spectral shape of emissions (obtained upon excitation at 360 and 315 nm, respectively) change considerably. On the other hand, efficient, pure monomer emissions were observed as expected in the devices-A from **1c**−**e**.

3.4. Pulse Radiolysis Studies. 3.4.1. Transient Absorption Properties. It has been established that radical cations of aromatic compounds are selectively formed during pulse radiolysis in 1,2-dichloroethane (DCE),[12] while radical anions are selectively generated in *N*,*N*-dimethylformamide (DMF).[13] In addition, absorption and emission behaviors from the recombination of incipient radical cations and radical anions can be measured upon radiolysis in benzene. To understand the nature of the in situ generated radical ions derived from these materials, DCE and DMF were also chosen for transient absorption measurements of their corresponding radical cations and anions, respectively, during the pulse radiolysis. It was found that the transient absorption bands (λ_{max}) and half-lives ($\tau_{1/2}$) of the resulting radical cations from **1a**−**e** fall in the ranges 540−630 nm and 1.0−35.4 μs, respectively (Table 3; see column-a in Figures 5 and 6). Notably, they are red-shifted and longer-lived progressively with increasing electron-donating nature of the C5 and C8 groups attached to the quinoxaline template.[14] In addition, both the radical cations from **1a** and **2a** exhibit the same transient absorption behaviors (λ_{max}: 540 nm, $\tau_{1/2}$ 2−3 μs, first two panels in column-a in Figure 5). On the other hand, essentially the same transient absorption profiles (λ_{max}: 610 ± 10 nm; $\tau_{1/2}$ ~10 μs) were also observed in DCE in the cases of **3f** and **4f** (last two panels in column-a in Figure 5).

For the transient absorptions taken in DMF, their incipient radical anions of **1a**−**e** with the absorption bands at ~510 nm are all long-lived (90−112 μs, see column-b in Figures 5 and 6). On the other hand, the transient absorption bands (λ_{max}) of the resulting radical anions of **3d**,**f** and **4f** are blue-shifted by 35−60 nm with the increasing electron-donating nature of the C3 and C7 groups. In marked contrast to those in **1a**−**e**, they are relatively short-lived ($\tau_{1/2}$ 0.7−2.1 μs).

Transient absorptions from the recombination of incipient radical cations and anions were taken in benzene and were quenched rigidly in the presence of oxygen. It is supposed that absorption bands (λ_{max}) in the range 530−745 nm from **1a**−**e** were assigned to be triplet absorptions to their lowest triplet excited states formed via energy transfer from ^{3}Bz* or charge recombination between radical ions, which is consistent with those observed at 580, 640, and 640 nm from **3d**,**f** and **4f**, respectively. In the cases of **1a** and **2a**, the same transient absorption band (λ_{max}) was observed at 540 nm. On the other hand, **3f** and **4f** exhibit the same behavior with the absorption

(11) (a) Yip, W. T.; Levy, D. H.; Kobetic, R.; Piotrowiak, P. *J. Phys. Chem. A* **1999**, *103*, 10. (b) Saragi, T. P. I.; Spehr, T.; Siebert, A.; Lieker, T. F.; Salbeck, J. *Chem. Rev.* **2007**, *107*, 1011.

(12) (a) Shida, T.; Hamill, W. H. *J. Chem. Phys.* **1966**, *44*, 2369. (b) Shida, T.; Hamill, W. H. *J. Chem. Phys.* **1966**, *44*, 2375. (c) Trapp, C.; Wang, C.-S.; Filler, R. *J. Chem. Phys.* **1966**, *45*, 3472. (d) Shida, T.; Kato, T. *Chem. Phys. Lett.* **1979**, *68*, 106. (e) Grimison, A.; Simpson, G. A. *J. Phys. Chem.* **1968**, *72*, 1776. (f) Ishida, A.; Fukui, M.; Ogawa, H.; Tojo, S.; Majima, T.; Takamuku, S. *J. Phys. Chem.* **1995**, *99*, 10808. (g) Majima, T.; Tojo, S.; Ishida, A.; Takamuku, S. *J. Org. Chem.* **1996**, *61*, 7793. (h) Majima, T.; Tojo, S.; Ishida, A.; Takamuku, S. *J. Phys. Chem.* **1996**, *100*, 13615.

(13) (a) Honda, E.; Tokuda, M.; Yoshida, H.; Ogasawara, M. *Bull. Chem. Soc. Jpn.* **1987**, *60*, 851. (b) Huddleston, R. K.; Miller, J. R. *J. Phys. Chem.* **1982**, *86*, 2410. (c) Majima, T.; Fukui, M.; Ishida, A.; Takamuku, S. *J. Phys. Chem.* **1996**, *100*, 8913. (d) Majima, T.; Tojo, S.; Takamuku, S. *J. Phys. Chem. A* **1997**, *101*, 1048.

(14) See the Supporting Information for CV stacked plots, emission spectra, and time-resolved transient absorption spectra of **1a**−**e**, **2a**, **3d**, **3f**, and **4f**.

Table 2. Electroluminescence Data of OLED Devices from **1a**−**e**, **3d**, **3f**, and **4f**

Device Configuration[a]	Em. λ_{max}[b] (nm)	V_{on}[c] (V)	η_{ext}[c] (%)	η_c[c]/η_p[c] (cd/A)/(lm/W)	L[c] (cd/m^2)	Literature Reference
1a/A	461, 548 (112)	3.9 (10.0)	0.20	0.60/ 0.24	964 (472)	---
1b/A	462, 562 (174)	2.5 (7.4)	0.09	0.22/ 0.13	445 (153)	---
1c/A	490 (70)	4.5 (4.9)	0.45	0.82/ 0.52	5995 (205)	---
1d/A	520 (82)	2.5 (4.0)	1.92	6.35/ 5.02	35372 (1268)	4
1d/B	524 (88)	4.7 (7.4)	1.06	2.90/ 1.19	11733 (414)	4
1e/A	576 (95)	2.8 (3.9)	0.98	2.54/ 2.05	23716 (524)	4
1e/B	580 (97)	3.9 (6.5)	2.90	7.75/ 3.73	20683 (1542)	4
1e/C	578 (96)	4.4 (6.3)	4.92	13.10/6.54	69700 (2503)	4
3d/D	434 (58)	3.3 (6.4)	1.89	1.38/0.68	1312 (274)	---
3d/E	420, 454 (62)	3.1 (7.4)	8.74	7.67/3.27	12722 (1520)	---
3f/D	462 (47)	2.9 (4.3)	1.94	2.90/2.10	12753 (595)	6
4f/D	440, 468 (70)	3.2 (4.3)	2.42	3.00/1.90	8939 (621)	6

[a] Device configuration **A**: ITO/NPB (40 nm)/**1a**−**e** (40 nm)/LiF (1 nm)/Al; **B**: ITO/**1c**−**e** (40 nm)/BCP (10 nm)/Alq (40 nm)/LiF (1 nm)/Al; **C**: ITO/NPB (40 nm)/**1e** (40 nm)/BCP (10 nm)/Alq (40 nm)/LiF (1 nm)/Al; **D**: ITO/**3d**, **3f** and **4f** (40 nm)/TPBI (40 nm)/LiF (1 nm)/Al; **E**: ITO/NPB (40 nm)/**3d** (40 nm)/TPBI (40 nm)/LiF (1 nm)/Al. [b] The data in parentheses correspond to full width at half-maximum (fwhm). [c] Turn-on voltage (V_{on}), external quantum efficiency (η_{ext}), current efficiency (η_c), power efficiency (η_p), luminance (L), and the data in parentheses of V_{on} and L were measured at 20 mA/cm^2.

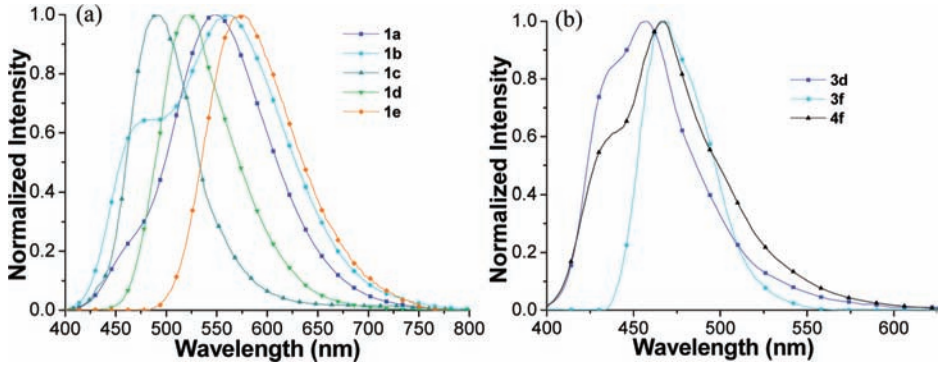

Figure 3. Stacked plots of EL spectra in the OLEDs from **1a**−**e** (Device-A) (a), from **3d** (Device-E), **3f**, and **4f** (Device-D) (b).

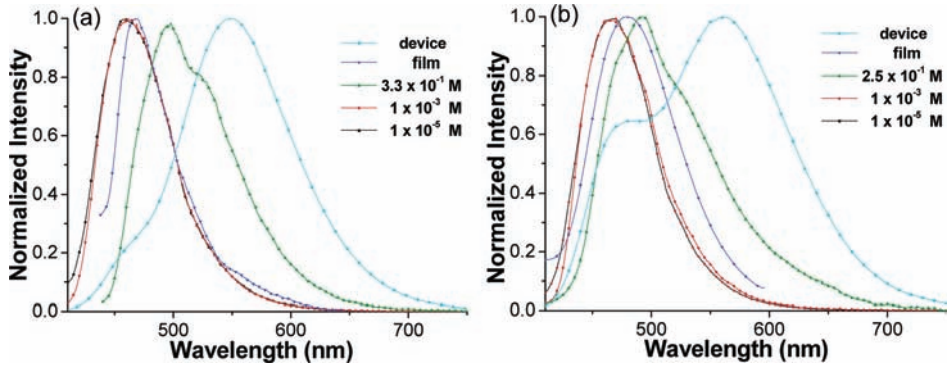

Figure 4. Stacked plots of emission spectra for **1a** (a) and **1b** (b) by steady-state measurements in Ar-saturated THF, film, and OLED device-A.

band (λ_{max}) observed at 640 nm, which is red-shifted by 60 nm in comparison with those for **3d**.

3.4.2. Radiolysis Induced Emission Properties. The emission spectra of **1a**−**e**, **2a**, **3d**, **3f**, and **4f** were taken during the pulse radiolysis in an Ar-saturated benzene solution (Figure 7). Notably, all these materials show only monomer emissions with lifetimes (τ_{fl}) of less than 8 ns. They all have similar emission wavelengths as those found by electroluminescence measurements (Table 2). Remarkably, it was found that there are relations between emission intensities observed during the pulse radiolysis in benzene and OLED performances. When **1e** was taken as a standard sample and compared individually to **1a**−**d**, **2a**, **3d**, **3f**, and **4f**, their relative emission intensity trend [**1d**,**e** (∼100%) ≫ **1c** (12%) > **1a**,**b** (∼4%) in Table 3)] is also consistent with the external quantum efficiency trend observed in their OLED devices (Table 2). Moreover, the emission efficiencies of each molecule in OLED device were proportional to the emission intensity obtained during the pulse radiolysis. For example, the relative emission intensities for **1d** (100%) and **1e** (105%) are ∼25 times stronger than that for **1b** (4%). Similarly, the external quantum efficiencies for **1d** (1.1−1.9%) and **1e** (1.0−2.9%) are ∼10−29 times stronger than that for **1b** (0.1%). On the other hand, the relative emission intensities for **3d**,**f** and **4f** are in the range 120−245%. Therefore, their external quantum efficiencies (1.9−2.4%) are ∼1−2.4 times stronger than that for **1d** (1.1−1.9%).

3.4.3. Electrochemical Properties and Annihilation Enthalpy Evaluation. The energy of the lowest singlet excited state (E_{s1}) for each materials can be calculated from the wavelength (λ_{max}^{Em}) of their respective emission maximum observed in

Table 3. Transient Absorption Peak (Abs. λ_{max}), Half-Life ($\tau_{1/2}$), Emission Peak (Em. λ_{max}), and Relative Emission Intensity (Em. Int.) Obtained during the Pulse Radiolysis for **1a**−**e**, **2a**, **3d**, **3f**, and **4f** in Ar-Saturated DCE, DMF, and Benzene Solutions

	in DCE		in DMF		in benzene		
Compd	Abs. λ_{max} (nm)	$\tau_{1/2}$ (μs)	Abs. λ_{max} (nm)	$\tau_{1/2}$ (μs)	Abs. λ_{max} (nm)	Em. λ_{max}[a] (nm)	Em. Int.[b] (%)
1a	540	2.9	510	70.3	540	468 (83)	3
1b	570	1.0	510	112.4	540	472 (80)	4
1c	580	4.2	510	112.4	530	483 (80)	12
1d	620	35.4	510	90.3	580	522 (95)	100
1e	630	8.6	530	94.1	745	574 (90)	105
2a	540	2.5	510	43.2	540	459 (78)	3
3d	600	10.2	600	2.1	580	450 (62)	171
3f	630	---	565	0.7	640	471 (68)	245
4f	620	10.0	540	2.0	640	464 (65)	120

[a] The values in parentheses correspond to full width at half-maximum (fwhm). [b] Emission intensity measured during the pulse radiolysis are determined from the total amount of emission relative to that of **1d** (100%).

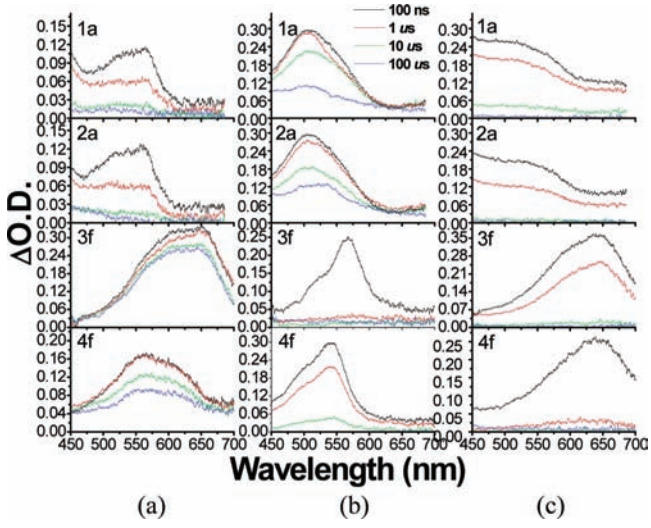

Figure 5. Time-resolved transient absorption spectrum stacked plots of **1a**, **2a**, **3f**, and **4f** observed at t = 100 ns (black), 1 (red), 10 (green), and 100 μs (blue) after an electron pulse during pulse radiolysis measurements in Ar-saturated (a) DCE, (b) DMF, and (c) benzene solutions.

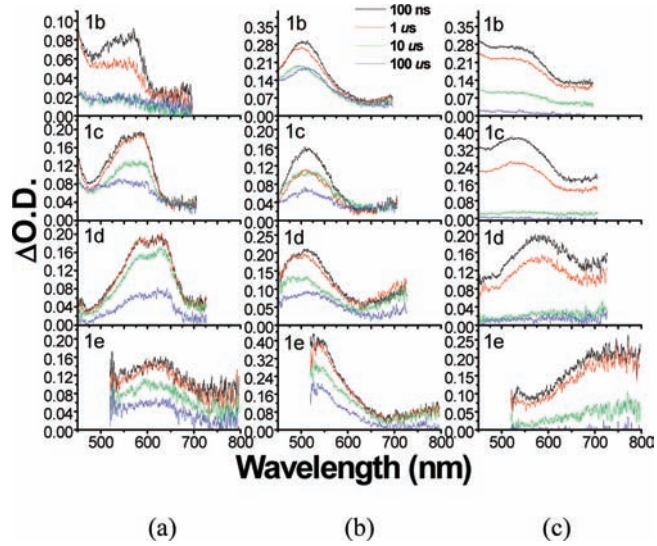

Figure 6. Time-resolved transient absorption spectrum stacked plots of **1b**−**e** observed at t = 100 ns (black), 1 (red), 10 (green), and 100 μs (blue) after an electron pulse during pulse radiolysis measurements in Ar-saturated (a) DCE, (b) DMF, and (c) benzene solutions.

benzene during the pulse radiolysis (Table 4). The longest absorption band-edge and the shortest emission one of organic compounds tend to overlap with varying extents. In some cases, molecules in their fully relaxed ground states have absorption at the region where their own emission was observed if the extent of overlap is more pronounced. Therefore, the self-absorption of the emission by its own ground-state molecule may be significant in steady-state photoluminescent measurements. Under such circumstances, the assessment of λ_{max}^{Em} may no longer be accurate enough due to changes in emission band intensity and shape. Nevertheless, the inaccurate calculation of λ_{max}^{Em} can be completely prevented by the pulse radiolysis measurements since the emission self-quenching can be shut down completely when the ground-state molecules are ionized and excited-state ones are formed through the charge recombination by electron pulse irradiation. Therefore, the E_{s1} values can be more correctly assessed. For example, the difference of λ_{max}^{Em} for **1e** between the steady-state (555 nm in benzene) and radiolytic (574 nm in benzene) measurements is −19 nm. On the other hand, the difference of λ_{max}^{Em} for **3f** between the steady-state (455 nm in benzene) and radiolytic (471 nm in benzene) measurements is −16 nm.

$$\Delta E = 1240/E_g(\text{nm}) \text{ and } E_{s1} = 1240/\lambda_{max}^{Em}\ (\text{nm}) \qquad (1)$$

The annihilation enthalpy change ($-\Delta H^\circ$) upon charge recombination of a given radical cation and radical anion pair provides an important insight to the nature of excited-state molecules responsible for the observed emission. The $-\Delta H^\circ$ values for **1a**−**e**, **2a**, **3d**, **3f**, and **4f** in benzene were calculated from their respective redox potentials and/or ΔE as shown in Table 4 according to the following eq 2:[15]

$$-\Delta H^\circ = \Delta E^{\varepsilon S} - \Delta G_{sol}^{\varepsilon S} - w_{a,u} + T\Delta S^\circ \qquad (2)$$

ΔE is the difference between its oxidation and reduction potentials of the solute material. ε_s, ΔG_{sol}, and $w_{a,u}$ represent the static dielectric constant of the solvent, the free energy change of solvation, and the work required to bring the radical cation and radical anion within a likely separation distance,

(15) (a) Gross, E. M.; Anderson, J. D.; Slaterbeck, A. F.; Thayumanavan, S.; Barlow, S.; Zhang, Y.; Marder, S. R.; Hall, H. K.; Nabor, M. F.; Wang, J.-F.; Mash, E. A.; Armstrong, N. R.; Wightman, R. M. *J. Am. Chem. Soc.* **2000**, *122*, 4972. (b) Elangovan, A.; Chen, T.-Y.; Chen, C.-Y.; Ho, T.-I. *Chem. Commun.* **2003**, 2146. (c) Elangovan, A.; Yang, S.-W.; Lin, J.-H.; Kao, K.-M.; Ho, T.-I. *Org. Biomol. Chem.* **2004**, *2*, 1597. (d) Elangovan, A.; Chiu, H.-H.; Yang, S.-W.; Ho, T.-I. *Org. Biomol. Chem.* **2004**, *2*, 3113. (e) Elangovan, A.; Kao, K.-M.; Yang, S.-W.; Chen, Y.-L.; Ho, T.-I.; Su, Y.-O. *J. Org. Chem.* **2005**, *70*, 4460. (f) Yang, S.-W.; Elangovan, A.; Hwang, K.-C.; Ho, T.-I. *J. Phys. Chem. B* **2005**, *109*, 16628.

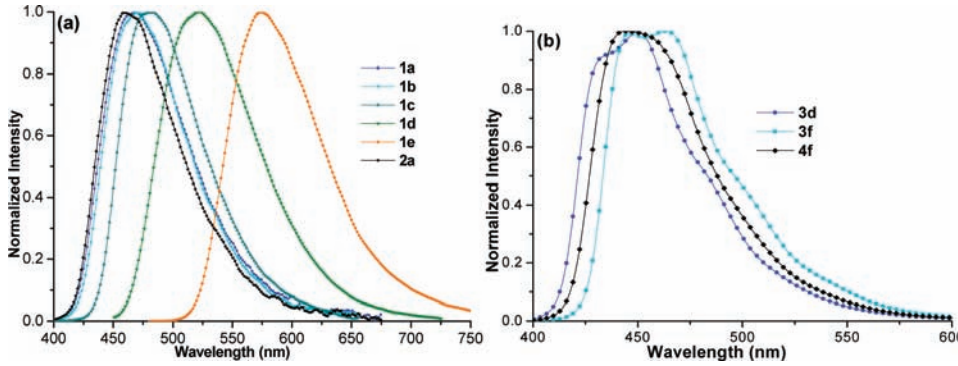

Figure 7. Fluorescence spectra of **1a**−**e** and **2a** (a), **3d**, **3f**, and **4f** (b) observed during the pulse radiolysis in Ar-saturated benzene solution.

Table 4. Electrochemical Properties, The Annihilation Enthalpy Change ($-\Delta H^{\circ}$), and Singlet Excitation Energy (E_{s1}) of **1a**−**e**, **2a**, **3d**, **3f**, and **4f** in Ar-Saturated CH_2Cl_2 and Benzene Solutions

	in CH_2Cl_2			in benzene		
Compd	E_{ox} [a](V)	E_{red} (V)	$-\Delta E$ (eV)	$-\Delta H^{\circ}$ (eV)	E_{s1} [d](eV)	$-\Delta H^{\circ} - E_{s1}$ (eV)
1a	N. A.	−2.03	2.90	3.03	2.65	+0.38
1b	N. A.	−2.01	2.84	2.97	2.63	+0.34
1c	N. A.	−2.07	2.79	2.92	2.57	+0.35
1d	N. A.	−2.07	2.66	2.79	2.38	+0.41
1e	+0.46	−2.05	2.51	2.64	2.16	+0.48
			(2.51)	(2.64)		(+0.48)
2a	N. A.	−1.95	2.96	3.09	2.70	+0.39
3d	+0.79	N. A.	2.98	3.11	2.76	+0.35
3f	+0.15, +0.32	N. A.	2.73	2.86	2.63	+0.23
4f	+0.34, +0.71	N. A.	2.87	3.00	2.79	+0.21

[a] Measured in CH_2Cl_2. [b] Calculated from band edge (5% intensity relative to that of the λ_{max}) wavelength of the longest wavelength absorption peak. [c] The data in parentheses are calculated as the difference between its redox potentials [$-(E_{red} - E_{ox})$]. [d] Calculated from the wavelength of the maximum emission peak.

respectively. In benzene, the expression for $-\Delta H^{\circ}$ can be simplified as in eq 3:

$$-\Delta H^{\circ} = E_{ox} - E_{red} + 0.13\ \text{eV} = -\Delta E + 0.13\ \text{eV} \qquad (3)$$

E_{ox} and E_{red} stand for the oxidation and reduction potentials of these matereials, respectively. They were determined by cyclic voltammetry experiments in CH_2Cl_2.[14] Notably, the annihilation enthalpy $-\Delta H^{\circ}$ calculated from both of the respective redox potentials is the same as that calculated from E_g as evidenced in the case of **1e**. Therefore, the annihilation enthalpy $-\Delta H^{\circ}$ calculated only from E_g in all the other cases should be reliable even with the lack of either E_{ox} or E_{red} data in the electrochemical measurements.

There is an increasing energy difference between $-\Delta H^{\circ}$ and E_{s1} in bipolar system **1b**−**e** (from +0.34 to +0.48 eV) progressively with increasing electron-donor nature at the C5 and C8 appendages. On the other hand, the difference is getting smaller with increasing electron-donor nature at the C3 and C7 substituents (from +0.35 to +0.23 eV) by comparing **3d** with **3f**. In addition, the energy difference varies in the cases of **1d** (+0.41 eV) and **3d** (+0.35 eV) with varying central optoelectronic templates (quinoxaline-fused DBE for system **1**; *cis*-stilbene for system **3**) despite the fact that they share the same donors (i.e., 4-methoxyphenyl).

4. Discussions

4.1. OLED and Transient Absorption Properties. The increasing transient absorption λ_{max} and time profiles of **1a**−**e** observed during the pulse radiolysis in DCE suggested that the electron-donating *para*-substituents at both C5 and C8 aryl appendages tend to stabilize and localize the incipient positive charges at the donor moieties. Similar transient absorption (λ_{max} 510−540 nm) and time ($\tau_{1/2}$ 2−3 and 43−70 μs) profiles were observed during the pulse radiolysis for both **1a** and the reference molecule **2a** without the spiral fluorene damper in three different solvents (DCE, DMF, and benzene). Similar transient absorption (λ_{max} 620−630, 540−565, and 640 nm) and time ($\tau_{1/2}$ 10 and 2 μs) profiles were also observed in the cases of **3f** and **4f**. These results strongly indicate that the fluorene damper does not play any role in stabilizing the incipient charges during the pulse radiolysis. The incipient positive and negative charges are located in the quinoxaline-fused DBE template (top template) for both **1a** and **2a** in DCE and DMF, respectively. Therefore, the intramolecular energy transfer from the perpendicular fluorene moiety to the quinoxaline-fused DBE template should not be involved and is not responsible for the observed emission in **1a**. A similar implication can be also applied to *cis*-bis(4,4′-*N*,*N*-diphenylamino)stilbene based **3f**.

In addition, all similar time profiles of the transient absorption (λ_{max}, 510−530 nm) during the pulse radiolysis in DMF for **1a**−**e** and **2a** indicated their incipient negative charges reside mainly at the quinoxaline heterocyclic moiety. On the other hand, the hypsochromic shifts of the transient absorption λ_{max} in DMF (from 600 nm for **3d** to 565 nm for **3f**) with increasing electron-donor property of the C3 and C7 substituents suggested that the central *cis*-stilbene moiety could not stabilize these incipient radical anions.

The $\tau_{1/2}$ values of the radical cations derived from **1a**, **1b**, and **2a** in DCE which correspond to the neutralization lifetimes by a chloride ion were found to be 2.9, 1.0, and 2.5 μs,

respectively. In this given family, they are significantly shorter than those of the radical cations for **1c**−**e** (4.2, 35.4, and 8.6 μs, respectively). Therefore, when the positive charges of the resulting radical cations for **1a** and **1b** are more localized to the terphenyl units in the top templates, the neutralization processes tend to be accelerated. Apparently, the neutralization occurs via the collision process between the incipient radical cations and chloride ion in DCE solution and is more facile in the former radical cations derived from **1a** and **1b**, which have larger collision cross sections than those of the latter ones. The $\tau_{1/2}$ values of the radical cations derived from **3d** and **4f** were found to be 10.2 and 10.0 μs, respectively. They are also significantly longer than those of the radical cations for **1a**, **1b**, and **2a**. Similar to **1d** and **1e**, the electron-donating groups in **3d** and **4f** tend to stabilize the incipient radical cations. Therefore, their neutralization processes appear to be slower when compared with those of the radical cations of **1a** and **1b**. On the other hand, the $\tau_{1/2}$ values of the radical anions of **1a**−**e** and **2a** are in the range 43.2−112.4 μs and significantly longer than those of the corresponding radical cations. These $\tau_{1/2}$ values also did not change considerably with increasing electron-donating nature of the appendages particularly in **1c**−**e**. The results are consistent with the presumption that the negative charges of the resulting radical anions mainly reside on the quinoxaline moieties in the top templates in **1a**−**e**.

Based on the time profiles of the transient absorption and device performance of these materials, it seems that the extent of local charge stabilization in a given material correlates well with its charge-transporting properties. It is known that charge transport from an electrode to the materials layer is favored for a matched HOMO or LUMO energy level between them in OLED devices. Among **1a**−**e**, **1d** and **1e** have shown the best performance efficiencies in OLED devices (entries 4−7, Table 2) as ET-type or HT-type fluorescent emitters. Apparently, the incipient positive or negative charges may be stabilized in the local electron-donating or electron-withdrawing quinoxaline moiety, thus facilitating the charge transports in the devices. In the cases of **1a**−**e**, their $\tau_{1/2}$ values measured in DMF solution were in the range 70.3−112.4 μs and can be treated as the ET-type emitters without resorting to the use of an extra ET layer in the OLED devices. On the other hand, the radical cations in DCE solution in the cases of **1d** and **1e** are reasonably long-lived (8.6−35.4 μs). Therefore, they can be treated as efficient HT-type emitters without resorting to the use of an extra HT layer in the OLED devices.

A similar explanation as that for **1d** and **1e** can also be applied to the cases of **3f** and **4f** which bear electron-donating groups in conjugation with the central *cis*-stilbene template. Since the $\tau_{1/2}$ value obtained in DCE in the case of **4f** (10 μs) is slightly longer than that for **1e** (8.6 μs),[16] **4f** can also be utilized as an efficient HT-type emitter in the devices. So far, **3d** is the only exception. Although the $\tau_{1/2}$ value for the incipient radical cation of **3d** (10.2 μs) is similar to that for **4f** (10 μs), the device performance by using **3d** as the HT-type emitter was not satisfactory (entry 9, Table 2). This issue could be understood in terms of the larger energy level difference (by 0.8 eV) between the work function of the ITO electrode (4.8 eV) and the HOMO energy level of **3d** (5.6 eV). This energy level mismatch causes a higher barrier toward the hole injection from the ITO to **3d** and thus results in poorer device performance. Nevertheless, much better device performance for **3d** can be achieved by inserting a hole transporting layer (i.e., NPB) between ITO and **3d** to facilitate the hole transport from the electrode as in device-E (entry 10, Table 2).

4.2. OLED and Transient Emission Properties. In both systems **1** and **3**, the emission profiles (emission wavelengths and relative emission intensities) observed during the pulse radiolysis in benzene were quite similar to their electroluminescence profiles. The results indicate that similar singlet excited states are involved as the emission species in both processes. In particular, there is a direct correlation on the trends of the emission intensities from both measurements. This highlights the possibility of evaluating the optoelectronic performance of given materials in OLED devices by first studying their transient emission profiles through pulse radiolysis experiments in benzene.

4.3. Annihilation Enthalpy Evaluation. As shown Table 4, $\Delta H°$ values for both systems **1** and **3** are larger than E_{s1}, suggesting that the energy available during the charge recombination is sufficient to populate the S_1 state. The increasing energy difference between $-\Delta H°$ and E_{s1} with the increasing bipolar nature of the materials in system **1a**−**e** indicates that their singlet excited states are more spontaneously generated down the series by the charge recombination (S-route) between incipient radical cations and anions of these materials. On the other hand, the central optoelectronic template in system **3** is not as competent an electron-accepting unit as that in system **1**. Therefore, the energy difference between $-\Delta H°$ and E_{s1} in system **3** decreases with the increasing electron-donating nature of the appendages at both C3 and C7 positions.

4.4. Emission Mechanisms in Pulse Radiolysis. No or negligible emission was observed during the pulse radiolysis of these materials in both DCE and DMF, which suggests that their incipient radical cations ($\mathbf{M}^{\bullet+}$) or radical anions ($\mathbf{M}^{\bullet-}$) do not emit light. In other words, both $\mathbf{M}^{\bullet+}$ and $\mathbf{M}^{\bullet-}$ must be formed at the same time to achieve the observed emission in benzene during pulse radiolysis.

Notably, the transient absorptions in the green to near-IR region of 530−745 nm observed during their pulse radiolysis in benzene can be readily quenched in the presence of oxygen or air. Their absorption decay by oxygen indicates the involvement of triplet excited states ($^3\mathbf{M}^*$) for these transient species. Therefore, these radical cations and anions recombine successfully to generate the corresponding singlet and/or triplet excited states within the electron pulse time span (i.e., 8 ns). Consequently, the emissions are resulted from the charge recombinations between respective radical cations and anions to form the singlet excited states which then relax to the ground states with concomitant release of fluorescent emissions.

Plausible pulse radiolysis-induced emission pathways in Ar-saturated benzene are summarized in Scheme 2. Radiolysis of benzene would lead to its radical cation ($\mathbf{Bz}^{\bullet+}$). The respective radical cations and anions are generated by reacting **M** with the in situ generated $\mathbf{Bz}^{\bullet+}$ and e^-, respectively. The charge recombination between radical cations and anions occurs to produce singlet ($^1\mathbf{M}^*$) and triplet ($^3\mathbf{M}^*$) excited-state molecules (eq 4, Scheme 2). These singlet excited states return to their ground states with concomitant release of emissions (eq 5, Scheme 2). Since the transient emission profiles of these materials correlate well with their optoelectronic performance profiles in OLED, we believe that such a recombination process

(16) The $\tau_{1/2}$ value of the radical cation for **3f** in DCE cannot be accurately measured because an unidentified intermediate was formed during the pulse radiolysis in DCE solution. Nevertheless, its $\tau_{1/2}$ value should be approximately the same as the $\tau_{1/2}$ value (10 μs) for **4f**.

Scheme 2. Fluorescent Emission Pathways during the Pulse Radiolysis of **1a**−**e**, **2a**, **3d**, **3f**, and **4f** in Benzene

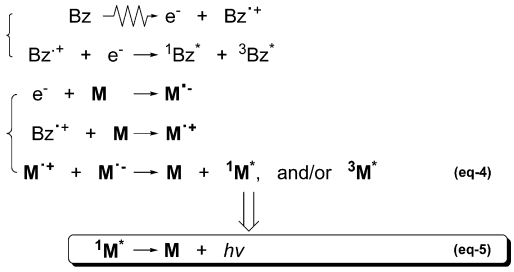

is very similar to the charge recombination of efficient bipolar emitting OLED materials with negligible interchromophoric contacts.

The charge recombination pathways described above require further elaboration. The radical cations and anions recombine with each other to form the excited-state molecules, which emit light during the pulse radiolysis and EL events. It is important to know how the individual positive and negative charges sustain in radical ions. Since similar absorption spectra were observed for the radical anions of **1a**−**e**, the incipient negative charges are assigned to be located in the electron-accepting quinoxaline, heteroaromatic moieties in the top templates of the radical anions derived from **1a**−**e**. On the other hand, the different transient absorption profiles obtained for the radical cations of **1a**−**e** suggest that the positive charges are not localized in the same functional group moiety in these top templates and are probably stabilized to different extents at both C5 and C8 appendages in all radical cations. The recent research work by Bard and co-workers provide some electrochemical evidence to support our presumption.[17]

Based on these findings, it seems that two different types of charge recombination mechanisms are involved for **1a**,**b** and for **1c**−**e**, respectively. In the cases of **1a** ($G = C_6H_5$) and **1b** ($G = 4\text{-}FC_6H_4$) with no or small *para*-substituents, the resultant radical cations are not stabilized by the H or F (an EWG group) at the *para*-postions of both the phenyl groups. Therefore, the positive charges need to be stabilized and delocalized through the terphenyl units in the quinoxaline backbones. The charge recombination may occur through intermolecular electron transfer with $\pi-\pi$ stacking from the radical anion ($\mathbf{M}^{\bullet-}$) with the charge residing in the quinoxaline moiety to the corresponding radical cation ($\mathbf{M}^{\bullet+}$) with the charge delocalized in the whole terphenyl unit (Scheme 3a). Moreover, the EL spectra of **1a**,**b** observed by charge recombinations were affected by self-absorption at a shorter wavelength region, thus resulting in the changes of emission spectral shapes.

In the cases of the radical cations derived from **1c**−**e**, however, the electron-donating *para*-substituents at both C5 and C8 aryl appendages can stabilize the incipient positive charges. The charge recombinations may occur through intermolecular electron transfer from the radical anion ($\mathbf{M}^{\bullet-}$) with the charge residing in the quinoxaline moiety to the corresponding radical cation ($\mathbf{M}^{\bullet+}$) with the charge localized in the electron-donating substituents (Scheme 3b). Notably, the resulting EL profiles for **1c**−**e** were not affected by self-absorption due to the lack of $\pi-\pi$ stacking at the terphenyl region of the quinoxaline backbone hindered by the *para*-substituents in G groups and more balanced charge transports. A similar mechanism could be illustrated for both **3d** and **3f** as that for **1c**−**e**. The charge recombination may occur through an intermolecular electron transfer from the radical anion ($\mathbf{M}^{\bullet-}$) with the charge residing in the whole *cis*-stilbene unit to the radical cation ($\mathbf{M}^{\bullet+}$) with charge localizing in the electron-donating appendages (Scheme 3c). Similar charge recombination mechanisms seem operative for the EL observed in OLED devices.

Scheme 3. Charge Recombination Mechanisms Proposed for (a) **1a** and **1b**, (b) **1c**−**e**, and (c) **3d** and **3f** through Electron Transfer from Radical Anion Moiety to Radical Cation Moiety

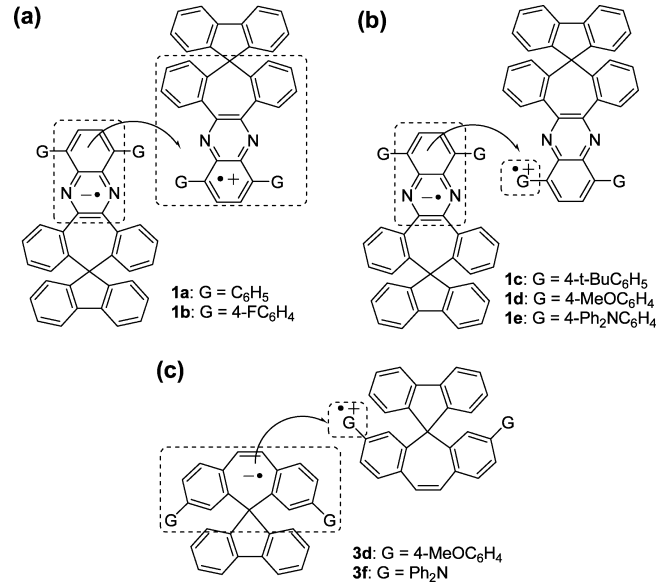

5. Conclusion

We have unraveled the origins of high optoelectronic performances for our recently developed molecular materials **1c**−**e** with integrated donor/acceptor moieties being through their efficient intermolecular charge recombination of incipient radical cations and anions to form the emissive singlet excited states. Bipolar molecules with discrete electron-donating and electron-withdrawing groups which possess an independent residing stability may achieve this purpose by their respective intrinsic charge stabilization property. In the cases of **1c**−**e**, **3d**, and **3f**, the individual singlet excited state is more smoothly formed, thus resulting in efficient fluorescent emissions by charge recombination pathways (Scheme 3b and 3c). The pulse radiolysis measurements for these compounds were found to be useful for indentifying or correlating the charge recombination processes both in solution and in the device. These transient absorption studies indicate that the local charge stabilization in the incipient radical cations and anions correlate well with the hole and electron transporting efficiency, respectively, of a given material observed in the device. By using the pulse radiolysis technique, one may come up with an ultimate structural materials design for which the device emission performance could be well predicted in advance. Hopefully in the near future, the pulse radiolysis technique allows us to predict the OLED performance of a new material by first looking at the transient absorption

(17) (a) Santhanam, K. S. V.; Bard, A. J. *J. Am. Chem. Soc.* **1965**, *87*, 139. (b) Keszthelyi, C. P.; Bard, A. J. *Chem. Phys. Lett.* **1974**, *24*, 300. (c) Lai, R. Y.; Kong, X.; Jenekhe, S. A.; Bard, A. J. *J. Am. Chem. Soc.* **2003**, *125*, 12631. (d) Choi, J.-P.; Wong, K.-T.; Chen, Y.-M.; Yu, J.-K.; Chou, P.-T.; Bard, A. J. *J. Phys. Chem. B* **2003**, *107*, 14407. (e) Fungo, F.; Wong, K.-T.; Ku, S.-Y.; Hung, Y.-Y.; Bard, A. J. *J. Phys. Chem. B* **2005**, *109*, 3984. (f) Rashidnadimi, S.; Hung, T.-S.; Wong, K.-T.; Bard, A. J. *J. Am. Chem. Soc.* **2008**, *130*, 634. (g) Izadyar, A.; Omer, K. M.; Liu, Y.; Chen, S.; Xu, X.; Bard, A. J. *J. Phys. Chem. C* **2008**, *112*, 20027.

profiles of the radical cation and anion and radiolysis induced emission through the charge recombination between them. The proposed dynamic tool augurs well for its potential applications toward probing decisive factors of achieving even more efficient optoelectronic materials.

Acknowledgment. We thank the members of the Radiation Laboratory of SANKEN, Osaka University, for running the linear accelerator and the National Science Council of Taiwan for generous financial support of this research. This work has been partly supported by a Grant-in-Aid for Scientific Research (Project 17105005 and others) from the Ministry of Education, Culture, Sports, Science and Technology (MEXT) of the Japanese Government.

Supporting Information Available: Experimental, device, spectrum, and photophysical measurement details for **1**−**4**. These material are available free of charge via the Internet at http://pubs.acs.org.

JA8090005